The role of ambient conditions on the performance of a planar, air-breathing hydrogen PEM fuel cell

Tibor Fabian [a,*], Jonathan D. Posner [b], Ryan O'Hayre [a], Suk-Won Cha [c],
John K. Eaton [a], Fritz B. Prinz [a], Juan G. Santiago [a]

[a] Department of Mechanical Engineering, Stanford University, Building 530, Room 226, Stanford, CA 94305, USA
[b] Department of Mechanical and Aerospace Engineering, Arizona State University, Tempe, AZ 85287, USA
[c] School of Mechanical & Aerospace Engineering, Seoul National University, Shilimdong, Gwanakgu, Seoul 151-744, Korea

Abstract

This paper presents experimental data on the effects of varying ambient temperature (10–40 °C) and relative humidity (20–80%) on the operation of a free-breathing fuel cell operated on dry-hydrogen in dead ended mode. We visualize the natural convection plume around the cathode using shadowgraphy, measure the gas diffusion layer (GDL) surface temperature and accumulation of water at the cathode, as well as obtain polarization curves and impedance spectra. The average free-convection air speed was 9.1 cm s^{-1} and 11.2 cm s^{-1} in horizontal and vertical cell orientations, respectively. We identified three regions of operation characterized by increasing current density: partial membrane hydration, full membrane hydration with GDL flooding, and membrane dry-out. The membrane transitions from the fully hydrated state to a dry out regime at a GDL temperature of approximately 60 °C, irrespective of the ambient temperature and humidity conditions. The cell exhibits strong hysteresis and the dry membrane regime cannot be captured by a sweeping polarization scan without complete removal of accumulated water after each measurement point. Maximum power density of 356 mW cm^{-2} was measured at an ambient temperature of 20 °C and relative humidity of 40%.
© 2006 Elsevier B.V. All rights reserved.

Keywords: Hydrogen fuel cell; Natural convection; Planar fuel cell; Air-breathing fuel cell; Dead-ended anode; Shadowgraphy

1. Introduction

Diffusion and free convection are the primary transport mechanisms for delivering oxygen to the cathode of air-breathing fuel cells. Air-breathing cells are typically characterized by low output power densities compared to forced-convection fuel cells [1–3]. They are nevertheless attractive for the portable-power applications where the simplicity of free-convection oxidant delivery can outweigh the cost, limited lifetime, reliability, complexity, noise, volume, weight, and parasitic power consumption of an auxiliary fan or compressor [4,5]. Balancing water in free-convection cells is challenging due the lack of control of ambient air stream conditions (flow stoichiometry, temperature, and humidity).

Mass transport at the cathode of an air-breathing fuel cell is driven by natural convection due to density gradients in the air. Air density gradients arise from temperature and chemical species gradients around the cathode. The density of air above the fuel cell cathode is a function of the local temperature, pressure, relative humidity, and oxygen partial pressure. Generally the cathode surface is warm and wet and conducts heat and diffuses water vapor to the surrounding fluid. Warm, humid, and oxygen starved air near the cathode has a lower density than the ambient air and drives buoyant flow with forces per unit volume of the form $F = g(\rho - \rho_{amb})$. Here g is the acceleration due to gravity, ρ is the density of the air in the point of interest, and ρ_{amb} is the density of the ambient air. These buoyant forces are balanced by viscosity and when a critical nondimensional Grashof number [6] is exceeded, natural convection develops which entrains fresh oxidant to the cathode. The operation of a free-convection cathode is therefore a complex coupling between heat and mass transfer at fuel cell/air interfaces.

* Corresponding author. Tel.: +1 650 723 7629; fax: +1 650 723 5034.
E-mail address: tfabian@stanford.edu (T. Fabian).

Early experimental studies of free-breathing fuel cells focused on fuel cells having cathode flow field plates with straight parallel channels with both ends opened to ambient air [1–3]. These investigations included studies of mass transport at the cathode [7], water balance [8], and current distribution [9]. The performance of this type of fuel cell is limited by mass transport at the cathode, and suffers from uneven current distribution due to humidity redistribution by the hydrogen and air flows. These cell designs tend to dry-out at high temperatures and low humidity and flood at high temperature and high humidity. The maximum reported power density at ambient conditions was approximately 70 mW cm^{-2}.

Planar air-breathing cells, similar to ones presented here, facilitate oxygen diffusion and advection of ambient air to the GDL surface by using a thin, stiff current collection plate that has a large open area [10,11]. Similar to the "open tube" design discussed above, experimental studies suggest that planar fuel cell performance can be severely limited by flooding. Power densities as large as 360 mW cm^{-2} have been reported [12] for planar air-breathing cells.

In this paper, we visualize the free convection air-flow at the cathode of a planar, air-breathing fuel cell by means of shadowgraph imaging. We characterize the cell performance as a function of ambient temperature and humidity. The fuel cell anode was operated using dry hydrogen gas in a dead-ended mode to simulate operating conditions in portable power applications where fuel efficiency and absence of auxiliary humidification units are crucial.

2. Experimental methodology

In this section we present the planar fuel cell design, the experimental setups for recording polarization curves, electrochemical impedance spectra, cathode temperatures, shadowgraph images, as well as the operation of the environmental control chamber.

2.1. Cell hardware

The fuel cell assembly is shown in Fig. 1. The outer dimensions of the system were 7 cm × 7 cm × 1 cm. The hydrogen feed chamber is a Delrin back-plate with two hydrogen distribution channels (each 5 mm wide, 5 mm deep, and 3 cm long). We use a printed circuit board (PCB)-based anode with 1.5 mm wide parallel flow channels spaced 1.5 mm apart [13,14]. We use a self-humidifying, Nafion 112-based 5-layer membrane electrode assembly (MEA) (BCS Fuel Cells Inc., Bryan, Texas) with 3 cm × 3 cm active area and 1 mg cm^{-2} catalyst loading on both sides. The uncompressed GDL thickness was about 400 μm. A 316 L stainless steel mesh coated with 10 μm Ni and 1 μm Au served as the cathode current collector. The top layer of the cathode is rigid PCB super structure with 16 square openings 6.4 mm wide. We deposit 66 μm of Cu, 10 μm Ni, and 1 μm Au on the PCB super structure to facilitate conductance and inhibit corrosion [15]. Eight bolts hold the assembly together and the torque on each bolt is 1 Nm. Silicone rubber gaskets placed between individual layers seal the anode compartment and provide for
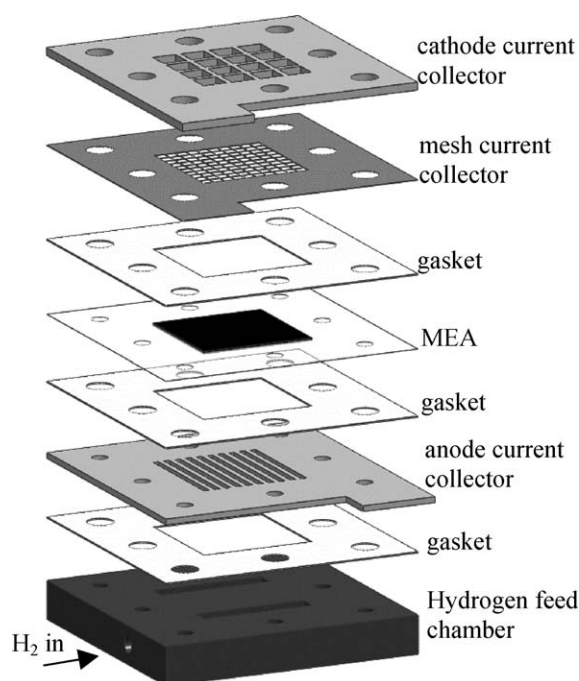

Fig. 1. Exploded view of the air-breathing fuel cell stack comprising anode feed chamber, parallel channel anode current collector, 3 cm × 3 cm active area MEA, current collecting mesh, and rigid cathode current collector.

optimal MEA compression. The uncompressed thickness of the gaskets between anode current collector and MEA, and cathode mesh and MEA was 380 μm, and 200 μm, respectively.

2.2. Thermal plume visualization

We visualized the plume of hot and humid gases near the fuel cell cathode using shadowgraphy. The intensity of shadowgraph images is proportional to the second spatial derivative of the index of refraction [16]. The refractive index of gaseous media is a function of the radiation wavelength, the gas density, and composition as expressed by the Gladstone–Dale Law. The index of refraction of humid air over the visible and infrared spectra is known very accurately due to its importance in meteorology. The index of refraction of humid air can be quantified using Edlén's equation [17] or more contemporary formulae [18,19]. The index of refraction is rather insensitive to the relative humidity of air. For example, using the formulae in [19] at 25 °C (assuming constant wavelength and ambient pressure), the difference in refractivity of dry air to air saturated with water vapor is smaller than the refractivity change due to a change in temperature of $\Delta T = 3 \times 10^{-7}$ °C. For this reason, the intensity variations in the shadowgraph images are largely due to variations in temperature and not water vapor content.

Fig. 2 shows a schematic of the shadowgraphy optical system. We used a continuous wave, single-line argon-ion laser (National Laser, Salt Lake City, Utah) as a 488 nm light source. We first expand and spatially filter the beam using a microscope objective and pinhole combination (Newport Corp., Irvine, CA). The diverging beam was collimated by the first of two 1.9 m
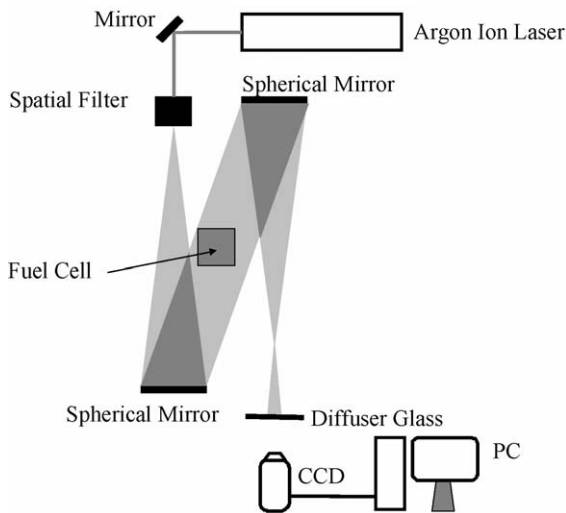
Fig. 2. Schematic of the shadowgraph imaging system. The intensity of shadowgraph images is proportional to the second spatial derivative of the index of refraction. A continuous wave, single-line argon-ion laser beam is expanded and spatially filtered using a microscope objective and a pinhole. The diverging beam is first collimated by the first concave spherical mirror, it passes through the field of interest, and finally it is focused by the second spherical mirror onto a diffuser glass where it is imaged by a CCD camera.

focal length concave spherical mirrors. The collimated beam passed through the field of interest and was focused by the second spherical mirror onto diffuser glass (Edmund Optics, Barrington, NJ). We recorded the images at a frame rate of $25\,s^{-1}$ with a 1024×1024 CCD camera (Cooke, Romulus, Michigan). The background external convection was minimized with a $300\,mm \times 300\,mm \times 300\,mm$ enclosure. The collimated beam entered and exited the enclosure through two $100\,mm$ diameter openings cut into the enclosure.

2.3. Environmental chamber setup

We evaluate the effects of the ambient temperature and humidity on the operation of the air-breathing cell by enclosing the cell in a controlled environment chamber. Fig. 3 shows the schematic of the experimental setup. It consists of the air-breathing fuel cell placed inside an environmental chamber (SM-3.5S, Thermotron, Holland, MI). The fuel cell anode compartment was fed with 99.999% pure dry hydrogen at a gauge pressure of 5 psi. The hydrogen flow was monitored with a flow meter (Series 16, Allicat Scientific Inc., Tucson, AZ). We controlled the operating point of the fuel cell with a computer controlled DC electronic load (6063B, Hewlett Packard, Palo Alto, CA). The electronic load was operated in a four-wire mode and required a 3.3 V boost power supply (W3.3MT65, Acopian, Easton, PA) [20]. The remote sense wires were connected directly to the fuel cell. We monitored the temperature of the fuel cell with a precision, fine-wire (0.003 in. diameter), K-type thermocouple (Omega Engineering, Stamford, CT) connected to an electronic cold-junction (Fluke 085, Fluke, Everett, WA), digitized by a data acquisition board (DAQPad-6020E, National Instruments, Austin, TX). A custom LabView script controlled the experiment and recorded the data. A potentiostat
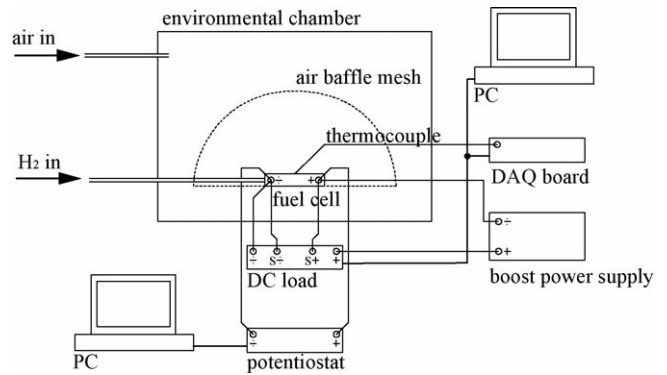

Fig. 3. Schematic of the experimental setup in an environmental chamber. The cell is surrounded by a hemispherical wire mesh shell to diminish the effects of forced convection inside the environmental chamber. Inside the chamber the air temperature and humidity were kept constant at a preset value. We fed cold, dry air into the chamber for improved humidity control and to retain constant partial pressure of oxygen. An active load controlled the operating point of the cell. The cell temperature was monitored by a thermocouple and cell impedance was measured with a potentiostat.

(PCI4/750, Gamry Instruments, Warminster, PA), connected to a second personal computer, measured the fuel cell impedance.

The environmental chamber simultaneously controls the temperature and humidity. The range of environmental conditions within the chamber is limited to a dewpoint of approximately $0\,^\circ C$. We feed the chamber with cold, dry air at a rate of approximately 10 slpm to reduce the dewpoint to nearly $-12\,^\circ C$. The air supply generates a positive airflow out of the chamber that inhibits ambient water vapor from diffusing into the chamber through the door seals or wiring ports. Finally, the external air-supply replenishes the oxygen inside the chamber consumed by the fuel cell during operation.

The environmental chamber has a fan that re-circulates the air inside the chamber and homogenizes the temperature and water vapor pressure. This forced convection affects the natural-convection at the cathode. We reduce the forced convection effects with a hemispherical enclosure, 30 cm in diameter, made of fine wire stainless-steel mesh surrounding the cell.

We evaluate the effects of forced convection in the environmental chamber on the performance of the cell by measuring polarization curves and impedance spectra. Fig. 4a shows polarization curves for the environmental chamber deactivated, with no air supplied, and the chamber door open to the ambient environment. A second polarization curve was recorded with the chamber door closed, with dry-air supply on, and the chamber set to the ambient temperature and relative humidity. The polarization curves differ less than 10 mV up to a current density of approximately $650\,mA\,cm^{-2}$. With further increase in current density the difference grows up to a maximum of 55 mV at $800\,mA\,cm^{-2}$. This marginal difference in cell potential is likely due to the improved mass transfer by the forced convection airflow around the fuel cell cathode. The ambient conditions during this experiment were $21\,^\circ C$ and 50% relative humidity.

We also measure the temperature profile across the cathode surface using a type-K thermocouple. The temperature distribution across the fuel cell surface was nonuniform and the temperature difference between the center and the edge of the
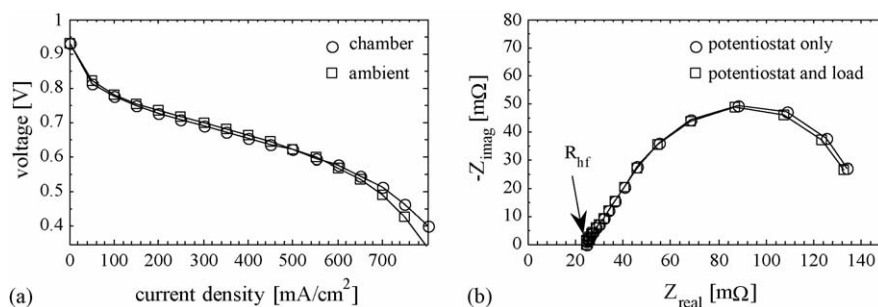
Fig. 4. (a) Overall effect of the environmental chamber on performance of the air-breathing cell under following conditions: 21 °C, 50% RH, Nafion 112 MEA with 1 mg cm^{-2} Pt loading, 30 s delay between each data point. (b) Effect of the input impedance of the active load on impedance spectra. The EIS measurements were performed with and without the active load. In both instances the fuel cell operating point was 450 mA at 806 mV and the excitation voltage was 10 mV.

open cathode was as large as 8 °C. To ensure reproducible temperature measurements we placed the thermocouple in the center of the same inner rectangular opening of the cathode superstructure in a direct contact with the cathode gas diffusion layer.

2.4. Electrochemical impedance spectroscopy

Electrochemical impedance spectroscopy (EIS) is a commonly used diagnostic tool for the investigation of fuel cell electrode processes. It measures system impedance by imposing a small magnitude sinusoidal voltage or current at a given operating point. The electrical current delivered by our air-breathing fuel cell exceeds the maximum DC polarization current of commercially available potentiostats. We circumvent this limitation by connecting the potentiostat in parallel with the fuel cell and the active load (see Fig. 3). During an EIS measurement the fuel cell was first loaded with a DC polarization current drawn by the active load operated in a constant current mode. Then, the potentiostat was set to potentiostatic mode at open cell voltage (OCV), corresponding to cell voltage at the DC load current, with 10 mV excitation voltage. Thus the active load drew the DC current and the potentiostat supplied the AC current. A disadvantage of this impedance measurement approach is that the AC current measured by the potentiostat is a sum of currents flowing through the fuel cell and through the DC load due to the finite input impedance of the load. Thus, the measured impedance equals fuel cell impedance in parallel with the input impedance of the active load.

We examined the influence of the DC load on the impedance measurement experimentally. First, the DC load was set to 450 mA. After 10 min stabilization the fuel cell potential settled to 806 mV and the first impedance spectra was recorded with the DC load connected in parallel to the fuel cell. Immediately afterwards, the DC load was disconnected from the fuel cell and a second impedance spectra was recorded. The potentiostat was operated in potentiostatic mode with the polarization potential set to 806 mV, matching the potential in the previous measurement with the active DC load. Fig. 4b shows the impedance spectra with and without the DC load in parallel. The two measurements deviate less than 3 mΩ at low frequencies. The impedance difference at low frequencies (right side) may be an effect of the load impedance as well as drift of the

fuel cell operating point. Overall, the effect of the DC load operated in the constant current mode on the EIS measurement is negligible at the impedances of interest.

We interpret the impedance spectra in accordance with previous work [21,22]. Generic fuel cell cathode impedance spectra include a curve with two arcs representing kinetic and mass transport losses. The first, high frequency arc represents kinetic losses due to oxygen reduction reaction (ORR) in the catalyst layer and the second, lower-frequency arc represents mass transfer losses due to diffusion of oxygen in the gas diffusion layer.

The typical impedance spectrum of an air-breathing fuel cell operating near OCV consists of a single, high frequency semicircle, similar to those shown in Fig. 4b. The intercept of the high frequency arc (left side) with the real axis (abscissa), R_{hf} corresponds to the total ohmic resistance of the cell. The ohmic resistance can be expressed as a sum of ionic resistance of the membrane, R_{ion}, and electronic resistance, R_{elec}, of the cell components: current collectors, cathode mesh, gas diffusion backings, catalyst layers, and the contact interfaces between them. The electronic resistance component is relatively constant and only marginally degrades over the lifetime of the components. We approximate the electronic resistance of the system as 11 mΩ by measuring the resistance of the stack without the Nafion membrane and assume that it remains constant during our experiments. The membrane ionic resistance is a strong function of the membrane water content and membrane temperature.

The typical impedance spectrum plots the negative imaginary part of cell impedance as a function of the real part of the cell impedance at a given operating point. The shapes and positions of impedance spectra vary depending on the cell operating condition. It is therefore difficult to compare impedance spectra for different operating conditions in a single plot. The most dramatic variation of the impedance spectra is due to changes in the ohmic resistance leading to large shifts of the impedance plots along the abscissa. We use a modified impedance plot where the negative imaginary part of the cell impedance is plotted as a function of the ohmic resistance-corrected real part of the fuel cell impedance. This allows for easy comparison of the kinetic and mass transfer arcs at different operating conditions.

The cell potential at a given operating point is affected by activation, kinetic, and ohmic loss mechanisms. We can visualize the kinetic and mass transfer losses independent of the ohmic

losses by plotting the IR-compensated potential as a function of current density. The IR-compensated potential is the measured potential plus the voltage drop due ohmic resistance, given as

$$V_{IR} = V + IR_{hf},$$

where V is the cell potential, I is the cell current, and R_{hf} is the total ohmic resistance. The slope of the IR-compensated polarization voltage as a function of current density is proportional to the low frequency intercept of the modified impedance spectra and represents the sum of the equivalent kinetic and mass transfer resistances [23].

2.5. Dead ended operation

The hydrogen flow rate at OCV was 0.3 sccm corresponding to approximately 4.5 mA cm^{-2} equivalent current density. This gas flow rate arises from hydrogen crossover through the Nafion membrane [24,25]. We observed no hydrogen leaks when we immersed the pressurized cell in a de-ionized water bath.

The anode compartment of dead-ended fuel cells must be periodically purged. Purging is required to remove product water, inert impurities present in the hydrogen, and the nitrogen diffusing from the cathode to the anode. The accumulated nitrogen decreases the partial pressure of hydrogen and therefore reduces fuel cell current density [26]. This effect can couple with fuel cell performance changes due to water imbalance and should therefore be avoided. We evaluated the effects of inert gas accumulation over a time period typical to a single experiment (approximately 2 h). We operated the fuel cell at a constant voltage of 0.85 V for a total time of 2 h. During this experiment, we purged the anode compartment for 3 s after 40 min and after 105 min. The immediate change of fuel cell current after the inert gas purge was less than 7 mA or 2% of the total fuel cell current.

2.6. Measurement procedure

A new MEA experiences a "break in" period where the resistance gradually decreases during the initial use [27]. We avoid biasing due to break-in period by conditioning each new membrane in the cell for 10 h at 0.5 V at an ambient temperature of 20 °C and relative humidity of 80%.

The fuel cell was conditioned prior to each experiment. First, we remove any condensed water by purging the anode compartment and cathode surface with dry air. Next, we purge the anode compartment with hydrogen and seal off the anode. At each environmental set point we place the fuel cell inside the chamber and operate the cell at OCV for 15 min followed by a 900 mA (100 mA cm^{-2}) constant current conditioning for 10 min.

We characterize the performance of the air-breathing fuel cell by *continuous* and *point-by-point* polarization scans. In a *continuous* scan, the fuel cell current increases by 450 mA steps (50 mA cm^{-2}) in 5 min intervals until the cell voltage drops below a certain threshold level, typically 0.4 V. After each current step, we allow the fuel cell voltage to stabilize and measure the cell potential and record an impedance spectrum. The duration of a single impedance spectrum measurement is about 1 min

and begins roughly 4 min after each current step. During the EIS measurements the potentiostat is operated in potentiostatic mode at the cell potential. The amplitude of the applied excitation voltage is 10 mV and the excitation frequency is varies from 10 kHz to 1 Hz. We record the fuel cell voltage and temperature over the entire duration of the scan.

In a *point-by-point* scan, the fuel cell current is increased in 900 mA (100 mA cm^{-2}) steps. Prior to each current set point the fuel cell is disconnected from the measurement apparatus, disassembled and both the cathode mesh as well as anode flow channels are purged with dry air. We reassemble the cell and weigh it on a microbalance (XE-510, Denver Instruments, Denver, CO). Next, we reconnect the cell to the measurement apparatus inside the environmental chamber, let the cell temperature and membrane humidity stabilize for 15 min, condition at 900 mA for 10 min, and operate the cell for 2 h at a constant current. After 2 h of operation the impedance spectrum is recorded. Finally, the fuel cell is disconnected from the measurement setup and weighed. We interpret the difference in weight before and after the run as a measure of the accumulated water. We record the fuel cell voltage and temperature over the duration of the entire scan. At higher current densities the fuel cell typically experiences a catastrophic dry-out within the 2 h time interval. In these cases we restart the measurement with the DC load operated in a constant potential mode. We set the cell potential to the voltage recorded at the last stable DC load current setting and repeat the measurement with 0.1 V voltage steps down to 0.4 V.

3. Results and discussion

In this section we first present shadowgraphy images of the thermal plume and measurements of the average plume velocity. Next, we present cell potential, GDL temperature, impedance spectra, and membrane resistance using the *continuous* scan over a wide range of environmental and operating conditions. We end this section with *point-by-point* measurements of the cell power density and accumulated liquid water over a range of environmental conditions.

3.1. Free convection visualization

Fig. 5 shows a representative series of shadowgraphy images of the plume surrounding the air-breathing fuel cell in the horizontal (top) and vertical (bottom) positions. The ambient conditions in the room were 25 °C and 35% relative humidity. The fuel cell was run in a potentiostatic mode at a cell potential of 0.4 V and a resulting current density of approximately 700 mA cm^{-2}. We measured an average, steady state cathode GDL temperature of 65 °C.

When the fuel cell was oriented with the cathode surface horizontal (in the *x–y* plane), we observed buoyant jets intermittently rise from the surface. The first few images in the top row of Fig. 5 show the start of one such event (near the surface) and dissipation of a jet already well away from the surface. Heat conduction as well as diffusion of water vapor and molecular oxygen from the cathode surface into the surrounding air
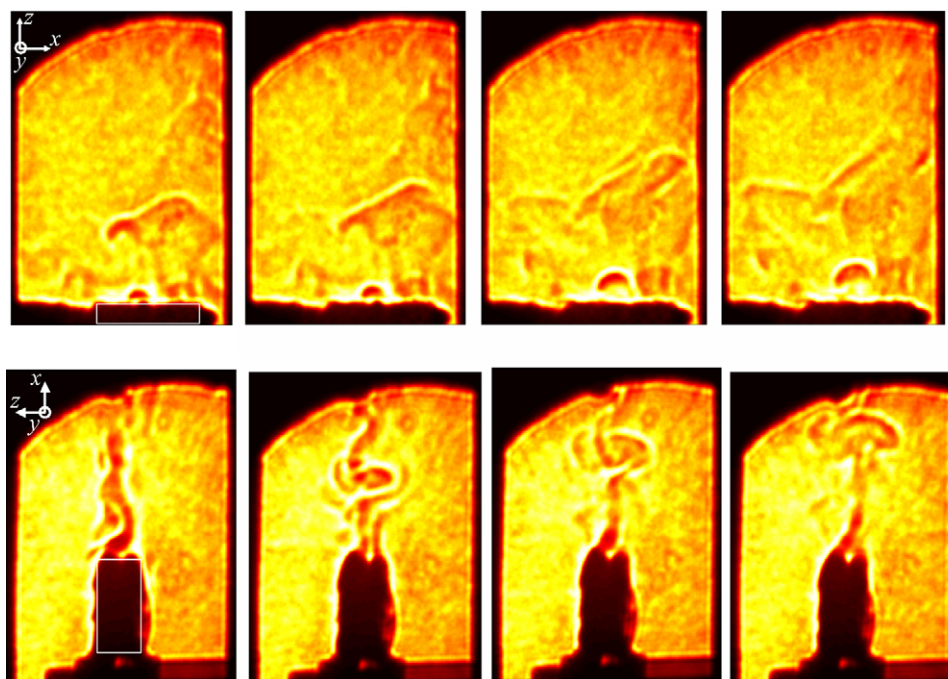
Fig. 5. Thermal plume shadowgraph visualizations of air-breathing fuel cell. The fuel cell boundaries are shown as a white box. The top row of images corresponds to a horizontal fuel cell cathode surface (gravity is in the negative z-direction). Buoyant plumes of hot, humid air convect upwards. The bottom row of images shows the case where the fuel cell surface is vertical (gravity is in the negative x-direction and the open cathode is facing in the positive z-direction). The majority of the experiments were performed in the horizontal orientation shown above.

provide for density gradients and therefore buoyancy forces, which are dissipated by viscous stresses. When the cell active surface was oriented perpendicular to gravity, plumes of hot, humid, and oxygen starved gases were periodically shed from the fuel cell surface at a rate of roughly $2.5\,\mathrm{s}^{-1}$. The observable gradients of these buoyant jets convected upwards at a velocity of about $9.1\,\mathrm{cm\,s}^{-1}$. We measured these velocities using a cross-covariance of a region of interest of consecutive shadowgraph images (top). The region of interest begins just above the cathode surface and extends to the top edge of the image. The pockets of hot, humid gas expanded in the x–y direction as they convected upward, and then appeared to "burst" and disperse into the ambient air. Each new plume was formed near the center of the cell (see the small dark hemispherical structure near the fuel cell surface in the first image of the top sequence).

When the cell cathode surface was oriented vertically (bottom of Fig. 5) the density gradients of the plume were much stronger and the plume was confined to a smaller region roughly corresponding to the $7\,\mathrm{cm}^2$ projected area (in the x-direction) of the fuel cell. In this orientation, the shear layers of the plume periodically rolled up into loose vortices. The vertical structures convected upwards at a velocity of roughly $11.2\,\mathrm{cm\,s}^{-1}$, marginally greater than those of the horizontal orientation. A greater buoyant velocity is expected in the vertical orientation because the same heat must be convected away from the cell surface by a smaller projected surface area (in respect to gravity). The measured natural convection velocities were on the same order as the forced convection velocities typically measured in indoor air spaces [28,29]. To our knowledge, this is the first shadowgraph visualization of natural convection around the cathode of a planar air-breathing fuel cell.

3.2. Effects of scan rate on cell potential and GDL temperature

The time interval at which the current density is stepped during a polarization scan affects the measured results. In particular, the stabilization time between changes in the current density must be long enough for the cell to reach steady state operation, which often results in long experiment durations. The time required to achieve steady state operation is a function of many factors including current density, ambient temperature and humidity, initial water content of the membrane, as well as the GDL properties, cell temperature, thermal mass of the fuel cell assembly, etc. We measured polarization data in *continuous* mode for stabilization time intervals of 10 s and 5 min as discussed in Section 2.6. Fig. 6a shows *continuous* polarization scans for 10 s and 5 min time intervals in the forward and reverse directions. The polarization curve recorded with 10 s between current increments shows strong hysteresis. The difference in fuel cell voltage between forward and reverse scan is as large as 60 mV at some current densities. The second polarization curve recorded with a 5 min delay between the current increments shows less than 15 mV hysteresis. The cathode GDL temperature for the two time intervals is shown in Fig. 6b. The average cell temperature hysteresis is $15\,^\circ\mathrm{C}$ and $4\,^\circ\mathrm{C}$ for the 10 s and 5 min time intervals, respectively.

We select the 5 min interval time for the remainder of the *continuous scan* experiments because it showed only marginal differences in the forward and reverse polarization scans. A single forward *continuous* polarization scan, including stabilization and conditioning, takes up to 2 h. Later, in Section 3.5, we present experiments with 2 h durations to study water accumu-
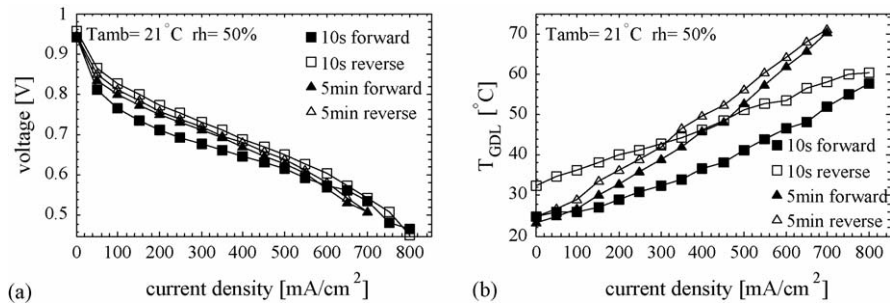
Fig. 6. Effect of 10 s and 5 min interval time on the continuous mode polarization curves (a) and the cathode GDL temperature (b). The ambient conditions were 21 °C and 50% relative humidity.

lation and membrane hydration. The quantitative data presented in this paper represents over 150 h of total cell run time.

3.3. Effects of ambient temperature and humidity on fuel cell performance

In this section we present results of the cell performance as a function of the ambient temperature and humidity. For each set of experiments we keep the temperature constant and vary the ambient humidity and operating conditions. Figs. 7–10 show the effect of ambient humidity on cell potential, cathode GDL temperature, and impedance spectra at ambient temperature of 40, 30, 20, and 10 °C, respectively. These data were recorded over a four day period. The chamber temperature was varied from 40 °C to 10 °C in 10 °C increments. During each day, the chamber temperature was kept constant and then decreased between measurement days. Each day four *continuous* polarization scans were recorded at relative humidity of 20, 40, 60 and 80%, respectively.

3.3.1. Humidity variations on fuel cell performance at 40 °C

At an ambient temperature of 40 °C the relative humidity has a strong impact on the fuel cell performance, as shown in Fig. 7a. This figure shows both measured potentials and IR-compensated potentials as a function of the current density. The fuel cell performance improves with increasing ambient humidity. The measured peak power increases from $250 \, \text{mW cm}^{-2}$ at 20% relative humidity to $310 \, \text{mW cm}^{-2}$ at 80% relative humidity. The IR-compensated polarization curves show only a marginal dependence on ambient humidity. The rapid drop in fuel cell potential at the end of the polarization scans is not apparent in the IR-compensated curves. This suggests that the ionic resistance of the membrane is the dominant loss mechanism at 40 °C.

Fig. 7b shows strong variation of the membrane resistance as a function of current density and relative humidity at 40 °C. The membrane resistance initially decreases with current density, reaches a minimum value, and then increases rapidly. The membrane resistance decreases due to membrane self-humidification
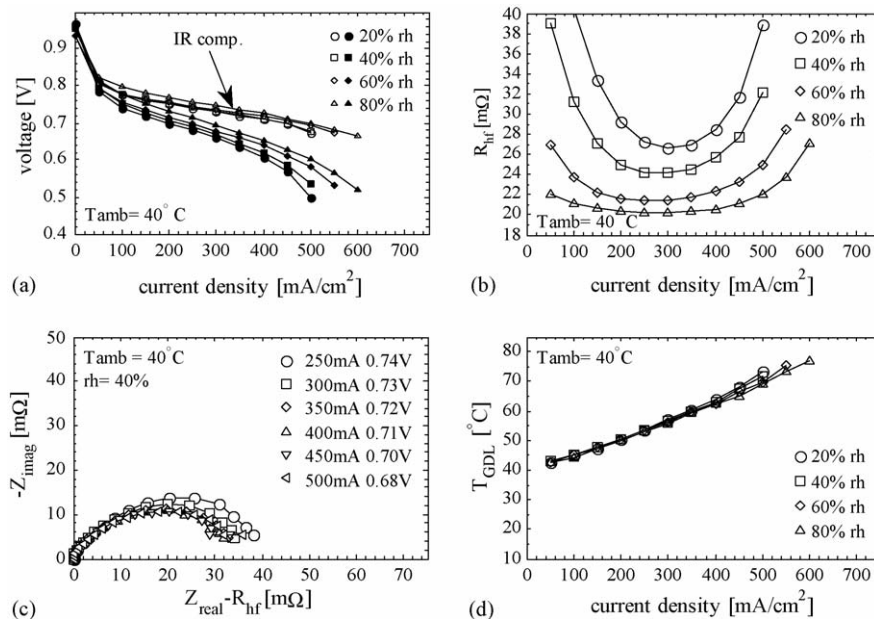

Fig. 7. Measured fuel cell data at 40 °C ambient temperature: (a) polarization (solid) and IR-compensated polarization curves (open); (b) high frequency resistance as a function of current density; (c) modified fuel cell impedance at 40% relative humidity, and with current density as parameter. The plot legend shows the current density and the IR-compensated fuel cell potential; and (d) GDL surface temperature.
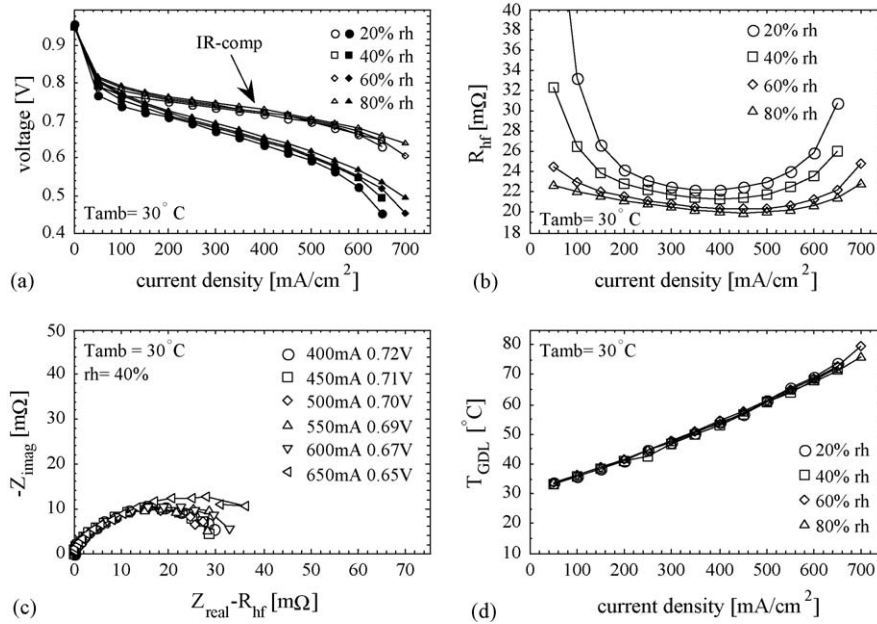
Fig. 8. Measured fuel cell data at 30 °C ambient temperature: (a) polarization (solid) and IR-compensated (open) polarization curves; (b) high frequency resistance as a function of current density; (c) modified impedance plot of fuel cell impedance at 40% ambient relative humidity, and with current density as parameter. The plot legend shows the current density and the IR-compensated fuel cell potential; and (d) surface temperature of the GDL as a function of current density.

with product water and self-heating with reaction heat. When the fuel cell current density exceeds approximately 300 mA cm^{-2} the GDL surface temperature equals or exceeds 55 °C (see Fig. 7d) and membrane resistance increases due to excessive evaporation from the cathode surface.

Fig. 7c shows a modified impedance plot for six of the larger current densities at a relative humidity of 40%. The impedance spectra at 40 °C consist of a single high frequency arc with

the exception of the impedance spectra obtained at 80% relative humidity where onset of second arc at the current densities above 550 mA cm^{-2} is observed but not shown here. Upon careful inspection, we observe a decrease in the radius of curvature of the high frequency arc when the current density increases from 250 to 450 mA cm^{-2}. The arc radius increases with further increase in the current density to 500 mA cm^{-2}. The radius of curvature of the high frequency arc is a measure of the oxygen

Fig. 9. Measured fuel cell data at 20 °C ambient temperature: (a) polarization (solid) and IR-compensated (open) polarization curves; (b) high frequency resistance as a function of current density; (c) modified impedance plot of fuel cell impedance at 40% ambient relative humidity, and with current density as parameter. The plot legend shows the current density and the IR-compensated fuel cell potential; and (d) surface temperature of the GDL.
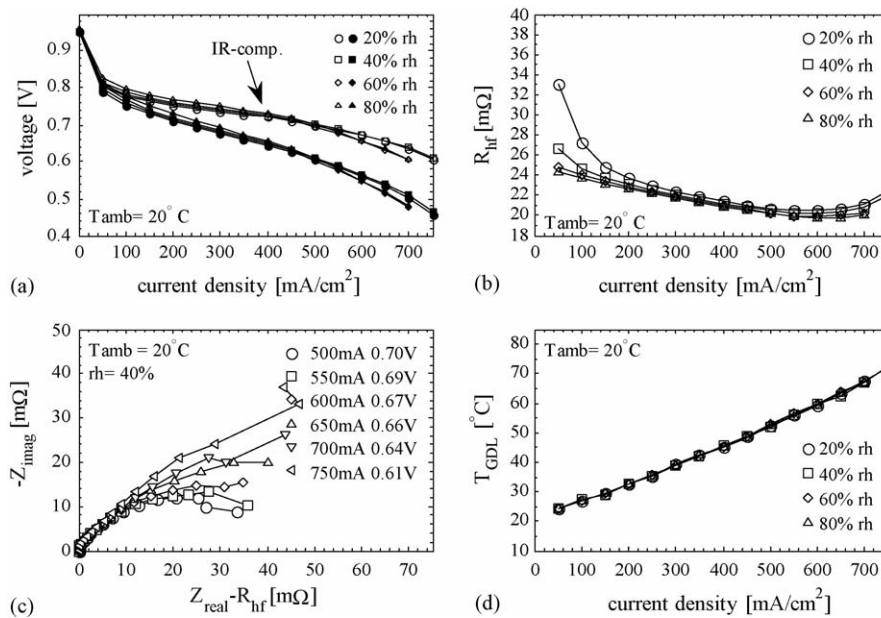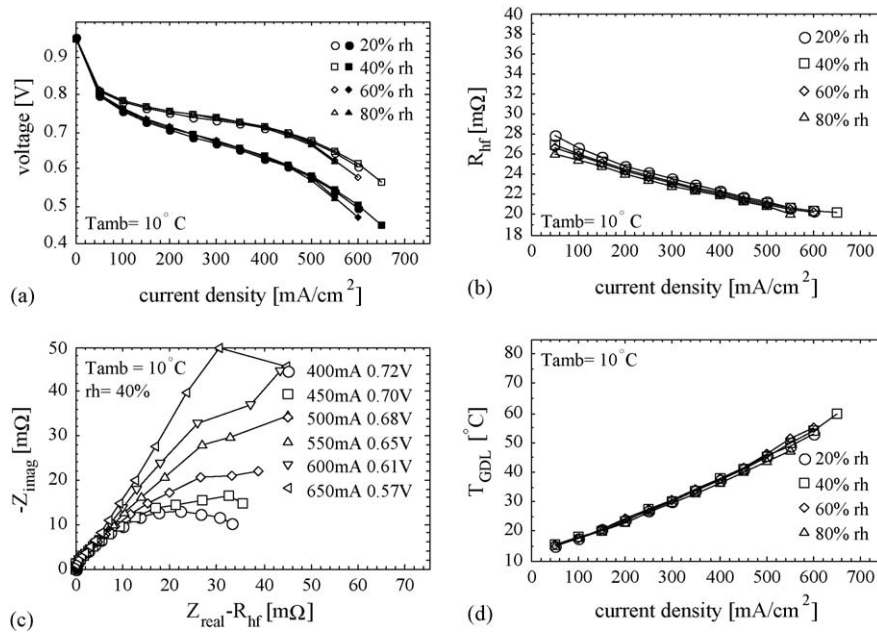
Fig. 10. Measured fuel cell data at 10 °C ambient temperature: (a) polarization (solid) and IR-compensated (open) polarization curves; (b) high frequency resistance as a function of current density; (c) modified impedance plot of fuel cell impedance at 10 °C ambient temperature, 40% ambient relative humidity, and with current density as parameter. The plot legend shows the current density and the IR-compensated fuel cell potential; and (d) GLD temperature as a function of the current density.

reduction reaction kinetic resistance and it is affected by the cathode overpotential as well as the oxygen concentration and the protonic conductivity in the catalyst layer [30]. Hence, both limited protonic conductivity in the catalyst layer due to insufficient catalyst ionomer humidification and low cathode oxygen concentration due to mass transport limitations increase the radius of curvature of the high frequency arc. A single large arc with a pronounced 45° angle at the high frequency intercept indicates a kinetic limitation due to decreased ionic conductivity in the catalyst. A large primary arc with the presence of a second arc indicates losses due to oxygen mass transport limitations. The modified impedance spectra shown in Fig. 7c consist of a single high frequency arc without any indication of a mass transport indicating second arc. This suggests that there are no mass transfer limitations at ambient temperatures of 40 °C, relative humidity of 40%, and current densities as large as $500 \, \text{mA cm}^{-2}$. The uniform radius of curvature of the high frequency arc is in agreement with the nearly constant slope of the IR-compensated polarization scan.

Fig. 7d shows the GDL surface temperature as a function of current density for four values of relative humidity. The temperatures overlap at low current density and diverge at higher current density. At higher current densities, we measure lower temperatures with increasing ambient humidity. This behavior is consistent with a more hydrated membrane, lower ohmic losses, and reduced joule heating.

3.3.2. Humidity variations on fuel cell performance at 30 °C

At an ambient temperature of 30 °C the impact of relative humidity on the overall fuel cell performance is less than at 40 °C. Fig. 8a shows polarization scans as a function of relative humidity. The cell performance improves with increasing ambient humidity as in the 40 °C case. The peak power increases from $314 \, \text{mW cm}^{-2}$ at 20% relative humidity to $348 \, \text{mW cm}^{-2}$ at 80% relative humidity. The IR-compensated polarization curves show minor dependence on ambient humidity. The slight change of slope of the IR-compensated curves at current densities above $500 \, \text{mA cm}^{-2}$ suggest kinetic and/or onset of mass transfer losses.

Fig. 8b shows the membrane resistance at 30 °C as a function of current density at four relative humidities. The membrane resistance behavior at 30 °C is similar to the 40 °C case. At 30 °C the cell reaches the minimum resistance at approximately $400 \, \text{mA cm}^{-2}$ (in contrast to $300 \, \text{mA cm}^{-2}$ at 40 °C). At this lower temperature, the region of low membrane resistance is broadened over a wider range of current densities and becomes insensitive to humidity at higher relative humidity. This result suggests that the membrane is fully humidified, hence insensitive to further ambient humidity increases, and the variation of membrane resistance is only due to changes in membrane temperature.

Fig. 8c shows a modified impedance plot for the six largest current densities of the polarization scan at an ambient temperature of 30 °C and relative humidity of 40%. The measured impedance spectra consist of a single high frequency arc with radius of curvature that initially decreases with increasing current density. However, at current densities above $550 \, \text{mA cm}^{-2}$ the onset of a second arc is visible, which is an indication of cathode losses due to oxygen diffusion in the gas diffusion layer. We present the surface temperature of the GDL as a function of current density in Fig. 8d. The temperature increases from 30 °C to 73 °C with current density. The temperature does not vary with humidity except at current densities exceeding $650 \, \text{mA cm}^{-2}$.

3.3.3. Humidity variations on fuel cell performance at 20 °C

At an ambient temperature of 20 °C the cell performs differently than at higher ambient temperatures. The polarization data in Fig. 9a shows that cell potential increases with increasing ambient humidity in the range of 20–40%. We attribute this increase to increasing membrane hydration. The cell potential decreases with further increases in ambient relative humidity in the range of 60–80%. The performance decreases at these higher humidities due to reaction product water flooding of the GDL. A flooded GDL inhibits the diffusive transport of oxygen to the cathode. We measure a peak power of 356 mW cm^{-2} at 40% ambient relative humidity. The IR-compensated polarization curves show improvement with increasing humidity in the first half of the polarization scan (at current densities below 450 mA cm^{-2}), suggesting improved protonic conductivity of the catalyst layer with increasing humidity. In the second part of the polarization scan, at current densities above 450 mA cm^{-2} the IR-compensated cell potential decreases with increasing humidity due to growing mass transfer impedance caused by the onset of flooding.

Fig. 9b shows membrane resistance as a function of current density at four discrete relative humidities and 20 °C ambient temperature. At this lower ambient temperature, we observe that the membrane resistance varies much less over the tested current density range as compared to membrane resistance at 30 °C and 40 °C. The resistance curves converge and remain relatively invariant over a wide range of current densities. The minimum resistance is located at approximately 600 mA cm^{-2} at a GDL surface temperature of approximately 59 °C. These results suggest that the membrane is well hydrated at moderate current densities and variations in membrane resistance are largely due to membrane temperature.

Fig. 9c shows a modified impedance plot for largest six current densities tested at the ambient temperature of 20 °C and relative humidity of 40%. The impedance spectra show characteristic mass transfer limitations where the high frequency radius of curvature increases with current density. We present the GDL surface temperature as a function of current density at four discrete ambient humidities in Fig. 9d. The temperature increases from 20 °C at OCV to 68 °C at current density of 700 mA cm^{-2}. At 20 °C the GDL temperature profiles do not vary with relative humidity.

3.3.4. Humidity variations on fuel cell performance at 10 °C

At an ambient temperature of 10 °C we observe that the fuel cell performance decreases with increasing ambient humidity, which suggests that the GDL is flooding. We measure a decrease in the peak power from 302 mW cm^{-2} at 20% relative humidity to 285 mW cm^{-2} at 80% relative humidity. The IR-compensated polarization curves show minimal dependence on ambient humidity in the first half of the polarization scan and mass transfer losses at current densities above 400 mA cm^{-2}. The IR-compensated polarization curves show a dramatic change of slope above about 400 mA cm^{-2} (see Fig. 10a).

Fig. 10b shows the membrane resistance as a function of current density at four discrete relative humidities. The resistance is approximately a linear function of the current density and no longer a function of ambient humidity. The minimum resistance is reached at a current density of about 650 mA cm^{-2} at a GDL surface temperature of nearly 59 °C. These results suggest that the membrane is well hydrated with product water and the variation of the membrane resistance is due solely to membrane temperature (see also Fig. 10d). The modified impedance data recorded at a relative humidity of 40% in Fig. 10c also show evidence of GDL flooding. Flooding is evident from an increase in arc radius with increasing current density.

The surface temperature of the GDL as a function of current density is shown in Fig. 10d. The plots for different relative humidity overlap over the entire range of measured current densities with slight variations at the highest current densities. The GDL surface temperature gradually increases from about 10 °C with the cell at OCV, to 59 °C at a current density of 650 mA cm^{-2}.

3.4. Role of temperature on cell performance

In this section we concentrate on the role of temperature on cell performance. Fig. 11 shows polarization scans and membrane resistances as a function of temperature and humidity. The data in these plots are obtained from the experiments presented in Section 3.3. The polarization curves in Fig. 11a show that at 20% ambient humidity the maximum cell power output is obtained at 20 °C. At lower temperatures (10 °C) the cell floods and at higher temperatures (30 °C and 40 °C) the cell dries out. The membrane resistance plots of Fig. 11b reinforce that the membrane dries out at low relative humidities and temperatures above 30 °C. At 40% relative humidity we observe only minor change in fuel cell performance as a function of temperature compared to operation at 20% relative humidity (see Fig. 11c). At this increased humidity, flooding at 10 °C is more apparent as indicated by a rapidly falling IR-compensated cell potential at high current densities. At 60% relative humidity the maximum fuel cell performance is obtained in a range of 20–30 °C (see Fig. 11e). Outside of this range there is a loss in cell potential due to flooding (lower temperatures) or insufficient membrane hydration (higher ambient temperatures). At 80% relative humidity we obtain maximum performance at 30 °C. At low current densities the membrane resistance decreases with increasing temperature as shown in Fig. 11h. The minimum resistance is a function of the ambient temperature. As we increase the ambient temperature the current density value at which the membrane resistance reaches a minimum decreases. At larger current densities (e.g. past the minimum resistance) the membrane dries out.

These results suggest that the rise in the cell temperature due to reaction heat and ohmic losses greatly affects the performance of the cell. The temperature difference between the GDL surface temperature, T_{GDL}, and the ambient air temperature, T_{amb}, is plotted as a function of produced fuel cell heat, Q_{tot}, in Fig. 12a. We define the fuel cell heat
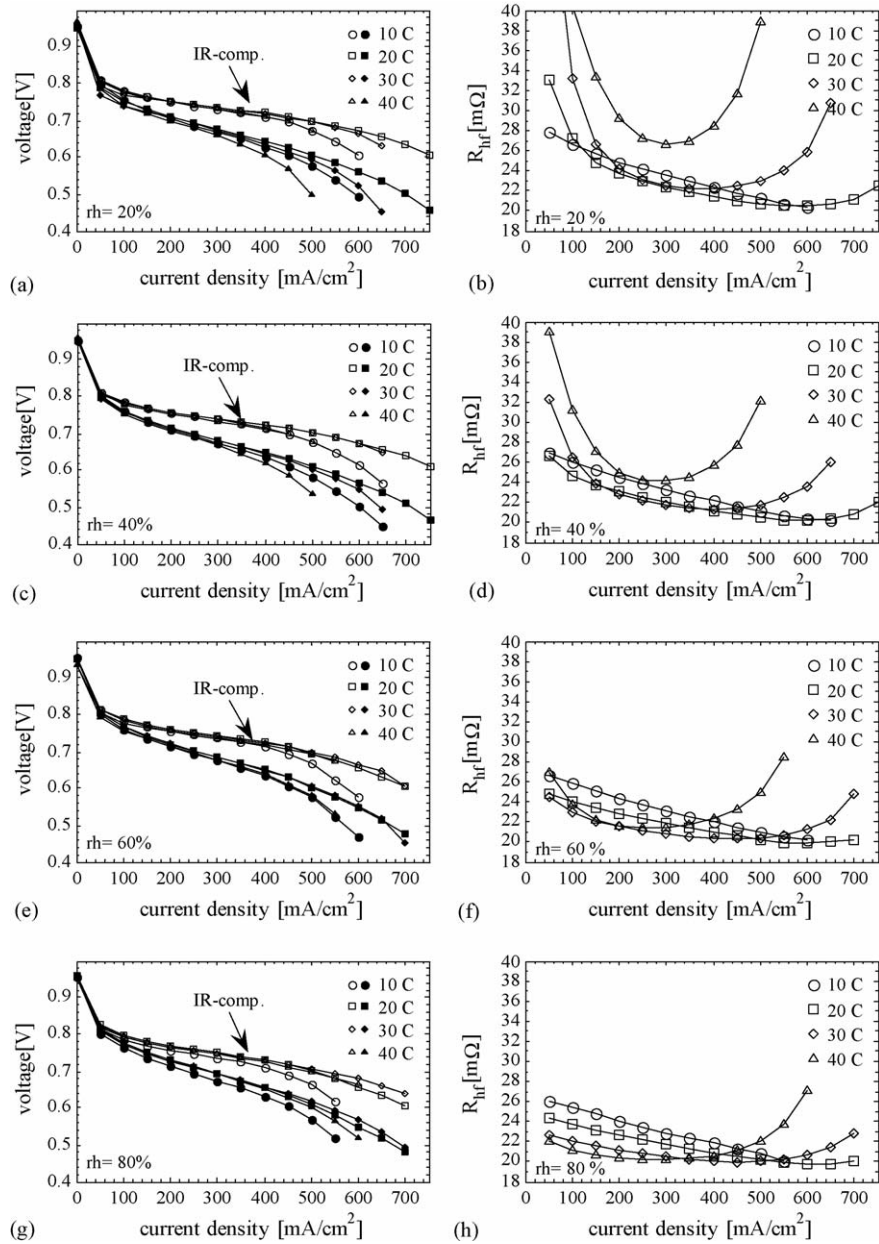
Fig. 11. Cell potential and high frequency membrane resistance, R_{hf}, as a function of current density at varying ambient temperature and humidity: (a, b) rh = 20%; (c, d) rh = 40%; (e, f) rh = 60%; and (g, h) rh = 80%.
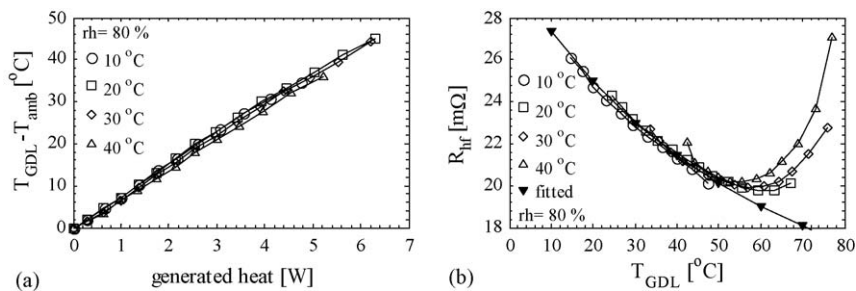

Fig. 12. (a) Temperature difference between GDL surface and ambient as a function of heat generated by the cell at 80% relative humidity and four ambient temperatures and (b) high frequency resistance as a function of GDL surface temperature, at 80% relative humidity and four ambient temperatures. The high frequency resistance is a good measure of membrane resistance and membrane hydration.

as,

$$Q_{\text{tot}} = \left(-\frac{\Delta H_{\text{rxn}}}{nF} - E \right) \times I \tag{1}$$

here E is the fuel cell voltage, I is the fuel cell current, n is the number of electrons transferred per mol in the reaction, F the Faraday constant, and ΔH_{rxn}, is the molar enthalpy of oxygen–hydrogen combustion reaction assuming the product water is a liquid. The slope of the plot in Fig. 12a is inversely proportional to the average heat transfer coefficient between the cell and the environment. The heat is transferred from the cell by natural convection at the bottom and at the top of the cell, by radiation from the cell surfaces, by conduction to the mesh on top of which the cell is placed, and by partial evaporation of product water from the open cathode surface. In theory, heat transfer rates due to radiation, natural convection, and evaporation increase with cell temperature. Our data suggests only weak dependence of the average heat transfer coefficient on surface temperature.

The cell self-heating dramatically impacts the membrane conductivity. Fig. 12b shows the ohmic resistance as a function of GDL temperature at 80% ambient relative humidity for four ambient temperatures. For temperatures between 10 °C and 60 °C the membrane is well hydrated with product water and the membrane resistance is, to a good approximation, only a function of the GDL temperature. In this range the membrane resistances collapse to a single curve and are not a function of the ambient temperature. At temperatures greater than 60 °C the resistance increases as the membrane dries out. Note that the minimum resistance value of 20 mΩ is reached at approximately 55–60 °C independent of the ambient temperature. We fit these results with the empirical Nafion conductivity model of Springer et al. [30], given as

$$R_{\text{hf}} = R_{\text{elec}} + R_{\text{ion}} = R_{\text{elec}}$$
$$+ \frac{t_{\text{mem}}}{A_{\text{mem}}\sigma_{30}\exp(1268((1/303) - (1/(273 + T_{\text{GDL}}))))} \tag{2}$$

where R_{elec} is the electronic part of the high frequency resistance, A_{mem} is the active area of the membrane, t_{mem} is the thickness of the membrane, σ_{30} is the membrane conductivity at 30 °C under full water saturation, and T_{GDL} is the membrane temperature. We measured the electronic resistance as 11 mΩ, the active membrane area as 9 cm^2, and use a Nafion 112 membrane thickness of 51 μm. Using σ_{30} as the sole fitting parameter we fit Eq. (2) to all of the data in Fig. 12b for temperatures below 50 °C. Using this method we estimate the Nafion 112 membrane ionic conductivity of 0.048 S cm^{-1} at 30 °C. The published values for proton conductivity of Nafion membranes vary considerably due to a variety of environments (H_2SO_4, water, water vapor, humidified gasses), temperatures (20–95 °C), experimental methods (DC, AC impedance spectroscopy) adopted during the conductivity measurements. For a recent review of published conductivity measurements see [31]. Our measured value may be biased towards lower conductivity due to temperature gradients along the membrane surface.

Fig. 12b shows that the membrane resistance deviates from the model at surface temperatures above approximately 55 °C. At these larger surface temperatures the cell tends to dry out. Above 60 °C the water flux due to evaporation from the GDL surface exceeds the water flux generated at the cathode, resulting in a dry membrane and an increase in membrane resistance. The cell experienced a thermal runaway when operated in constant current mode and when surface temperature due to self-heating exceeded the critical dry-out temperature of approximately 55–60 °C. As the GDL surface temperature exceeded 60 °C the membrane water content decreased and resulted in an increase of membrane resistance, which in turn increased the amount of generated heat and consequently the GDL surface temperature. Consequently, the cell voltage rapidly collapsed due to rapid increase in membrane resistance.

3.5. Water accumulation

In this section we investigate water accumulation in the dead-ended, air-breathing fuel cell with *point-by-point* polarization scans. The relative humidity was kept constant at 40% while the ambient temperature was varied from 10 °C to 30 °C in 10 °C steps.

Fig. 13 compares fuel cell potential, high frequency resistance, and GDL temperature obtained by the *continuous* polarization scan (5 min stabilization between data points) and the *point-by-point* polarization scan (2 h operation at each operating point with water purge after each measurement point). The dotted lines in the polarization plots represent fuel cell operating points with heat losses that result in a GDL surface temperature of approximately 60 °C. The area to the right of the isothermal line is the regime of where the cell membrane dries out.

Fig. 13a shows that the *point-by-point* polarization scan overlaps with the continuous scan at 10 °C and current densities of 200 mA cm^{-2} or less. In the range of 200–600 mA cm^{-2}, the 2 h measurements drop slightly below the continuous scan. At current densities greater than 600 mA cm^{-2} the cell operated in *continuous* mode outperforms the cell operated in the *point-by-point* mode. At current densities between 200 mA cm^{-2} and 600 mA cm^{-2} the cathode is severely flooded during the 2 h operation time. Water accumulation at the cathode occurs in several phases. First, small water droplets condense on the cathode mesh typically along the edges of the super structure openings. The droplets grow in size and eventually coalesce into a single large droplet roughly centered at each cathode opening. In some cases, these larger droplets fully block the super-structure openings. For the *point-by-point* scan and at current densities in excess of 600 mA cm^{-2}, self-heating leads to faster evaporation, reduction of cathode flooding, improved mass transfer and the *point-by-point* scan outperformed the *continuous* scan. At current densities above 700 mA cm^{-2}, the membrane begins to dry out and the high frequency resistance increases. In the continuous scan mode the membrane does not dry out at these high current densities since the cell has stored water from the measurements made at lower current densities.
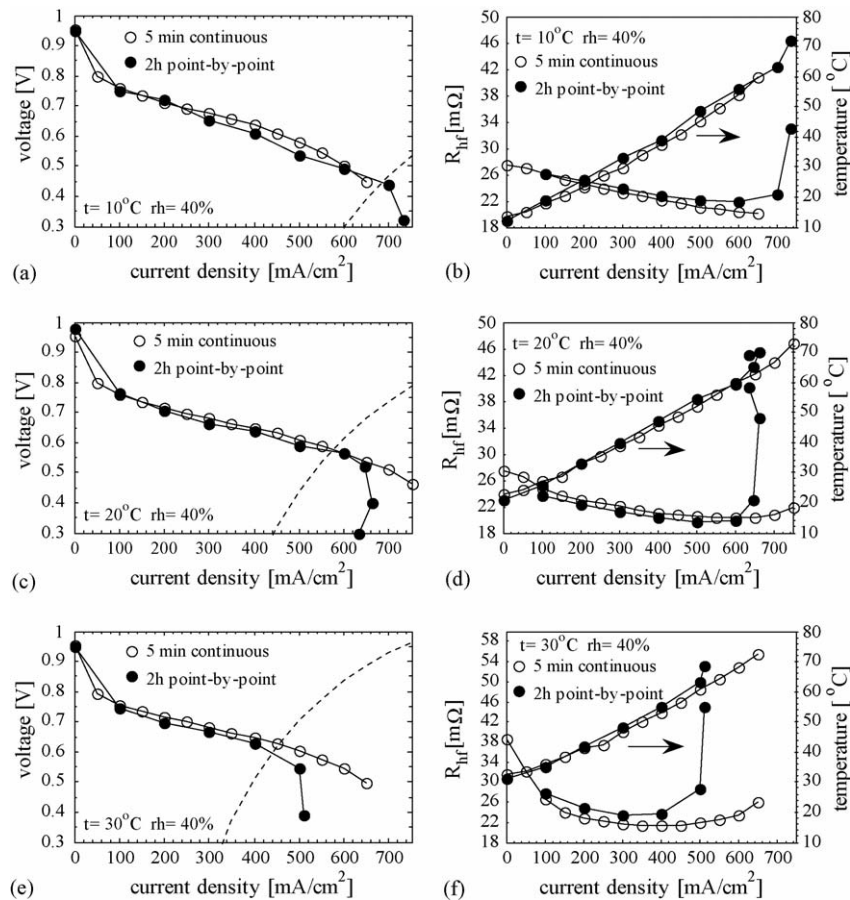
Fig. 13. Comparison of IV curves, GDL temperature, and high frequency resistance obtained with a *point-by-point* and *continuous* polarization scans at a relative ambient humidity of 40% and varying ambient temperatures: 10 °C (a, b); 20 °C (c, d); and 30 °C (e, f). Dotted line in a, c, and e indicates isotherm where the surface temperature due to self-heating reaches 60 °C.

Fig. 13(c) and (e) show that at 20 °C and 30 °C we observe a reduction in the cell potential at larger current densities as the membrane dries out. As is presented for the 10 °C case, the cell dries out when it reaches 60 °C. Fig. 13(c)–(f) show that the cell reaches 60 °C (shown as dotted isotherm in (c) and (e)) at progressively lower current densities as the ambient temperature increases. In Fig. 13c, the cell reaches 625 mA cm^{-2} at both 0.55 V and 0.3 V. The operating point at 0.3 V was obtained by operating the cell in potentiostatic mode. The *continuous* scans fail to capture the rapid membrane drying at high current densities measured by the *point-by-point* scan. The continuous scan over predicted cell performance under ambient conditions where water condensation occurred at medium current densities. The condensed water stored on the cathode surface as well as in the anode manifold transiently improved the cell performance in *continuous* scans where dry-out occurred in *point-by-point* scan. Increasing the time between current increments during the *continuous* scan will not resolve this problem, since longer dwell time between current increments will lead to proportionally more condensed water stored in the fuel cell. These results show that the performance of the cell is operation path dependent. Therefore it is important to consider the operation history of the cell when interpreting fuel cell data.

Fig. 14a shows the measured volume of condensed water after 2 h of operation at each operating point of the cell using the *point-by-point* mode. The amount of condensed water increases with current density, reaches a maximum, and then quickly drops to zero. Large volumes of water suggest that the cell is flooding. Each data point in Fig. 14a is labeled with a percentage value of accumulated water. This percentage of condensed water is
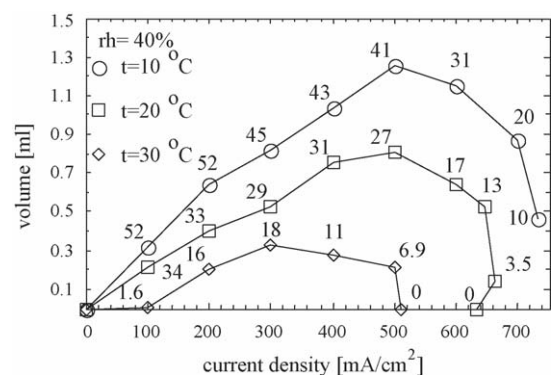

Fig. 14. Volume of water condensed in the fuel cell after 2 h of operation at each operating point. The labels next to the data points represent the amount of condensed water as a fraction of the produced water at each operating point. Accumulated liquid water volume was deduced from weight measurements.
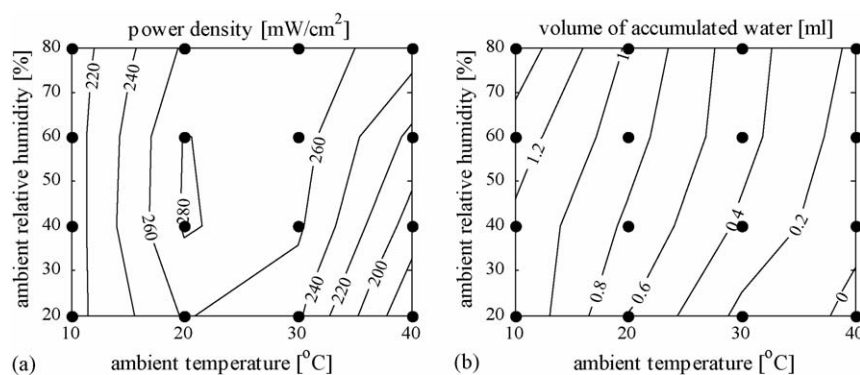
Fig. 15. Contour map of power density: (a) condensed water volume and (b) after 2 h of operation as a function of ambient temperature and humidity. The values were measured at discrete operating conditions denoted by the circle markers. The power density reaches a maximum at an operation point between 40% and 60% relative humidity and near $T = 20\,^{\circ}C$. Power density is limited by dry-out at high temperatures and by flooding at low temperatures. The accumulated water volume is a strong function of ambient temperature and increases with decreasing temperature.

measured as the accumulated water normalized by the amount of water that is theoretically generated by the cell during 2 h of operation at a given current density. This fraction is expressed by

$$\frac{m_a}{t(I/nF)M_{H_2O}}, \tag{3}$$

where m_a is the weight of accumulated water, t is the duration of experiment, I is the time averaged cell current, n is the number of electrons transferred per mol of reaction, F is Faraday's constant, and M_{H_2O} is the molecular weight of water. At $10\,^{\circ}C$, nearly 50% of the product water condenses, at $20\,^{\circ}C$ approximately 30% condenses, and at $30\,^{\circ}C$ only 17% condenses. The location of water condensate was not restricted to the cathode surface but also occurred in the anode gas manifold. In fact, the anode condensation occurred in areas closest to the outer corners of the fuel cell where the temperatures are lowest. We could not distinguish the anode and cathode contributions to the total accumulated water. Note that both the anode and cathode condensate is a consequence of thermal gradients, flow field, and operation, and strongly depends on the cell design and coupling with the ambient conditions.

Finally, we investigate the effect of ambient conditions on fuel cell performance at a constant operating voltage of 0.6 V. We run the fuel cell for 2 h at ambient temperatures of 10, 20, 30 and $40\,^{\circ}C$ and at relative humidities of 20, 40, 60, and 80%. Fig. 15a shows a contour map of power density measured as a function of the ambient temperature and humidity that was extrapolated from the measurements (measured data points shown as solid circles). The power density map shows a $260\,mW\,cm^{-2}$ plateau region at temperatures between $20\,^{\circ}C$ and $30\,^{\circ}C$. The cell achieves a maximum power of $300\,mW\,cm^{-2}$ at $20\,^{\circ}C$ and humidities from 40% to 60%. Note that the optimal ambient conditions correspond to typical indoor air conditions of $20\,^{\circ}C$ and 50% humidity. The power density is mostly a function of ambient temperature and only a weak function of ambient relative humidity. The power density was limited by dry-out at temperatures above $30\,^{\circ}C$ and by flooding below $20\,^{\circ}C$. The membrane dry-out was exacerbated by low ambient humidity. These power values are not the maximum the cell can produce, but serve to

demonstrate how ambient conditions govern power at a single load condition.

Fig. 15b shows the condensed water volume as a function of ambient temperature and humidity. The water volume increases with decreasing ambient temperature and increasing ambient relative humidity. At $40\,^{\circ}C$ ambient temperature there is approximately no condensation while at $10\,^{\circ}C$ the cell is flooded. These results suggest that more water is evaporated from the cell surface in dry and hot ambient conditions.

4. Conclusions

We have presented an experimental investigation of a free-breathing, hydrogen fuel cell at varying ambient temperature and relative humidity. Mass and heat transfer at the cathode surface occurs predominantly by natural convection. Shadowgraph flow visualization of the unsteady thermal plume above the cathode shows that pockets of warm humid air are shed from the cell 2.5 times per second with a velocity that depends on the orientation of the cell ($9.1\,cm\,s^{-1}$ in horizontal and $11.2\,cm\,s^{-1}$ in vertical cathode surface orientation). The plume's velocity is comparable to naturally occurring flows in a laboratory environment and suggests that forced convection due to slight room currents is an important factor in air-breathing fuel cell mass and heat transfer.

The performance of the free-breathing cell is dependent on the membrane electrode assembly water content. The net water balance of the cell is a complex coupling of cell self-heating and water production as well as the convection of heat and water vapor to the environment. We identified three regions of fuel cell operation, which are characterized by the membrane hydration level (listed in order of increasing current density): partial membrane hydration, full membrane hydration with GDL flooding, and membrane dry-out. We find that the membrane transitions from well hydrated to dry at a critical GDL temperature of approximately $60\,^{\circ}C$. The $60\,^{\circ}C$ transition temperature is the condition at which the water removal due to evaporation balances the water generation rate due to reaction. This critical transition temperature is nearly independent of ambient conditions as the evaporation rate is an exponential function of the

GDL temperature while the water generation flux increases linearly with temperature.

Although the critical membrane transition temperature does not depend on the ambient conditions, the current density at which the cell reaches the critical temperature does depend on the ambient temperature and humidity. As the ambient temperature increases, the current density required to reach the critical GDL temperature decreases. When the ambient is warmer, the cell rejects less heat and the GDL temperature increases. At high temperature and low relative humidity the membrane dries out, and the cell potential drops rapidly at higher current densities. At low temperature and high relative humidity the cell floods at high current density.

Ambient conditions impacted all three major electrochemical loss components of the air-breathing fuel cell: activation, resistive, and mass transfer. Activation losses were typically the largest loss component. However, these were affected negligibly by varying ambient conditions. A small increase in activation losses was observed at high ambient temperature and low humidity (probably due to catalyst dry-out). Resistive losses were most strongly affected by ambient conditions and dominated fuel cell losses during dry-out at high current densities. Mass transfer losses typically became important above about $400 \, \text{mA cm}^{-2}$. Furthermore, low ambient temperatures, and high ambient humidity both tended to increase mass transfer losses due to flooding of the GDL.

We found that *continuous* polarization scans (even at slow scan rates) fail to capture the rapid membrane drying at high current densities measured by the *point-by-point* scan. The *continuous* scan over predicts the cell performance because of the water stored in the fuel cell assembly at moderate current densities. The *point-by-point* scan procedure that allows for complete removal of accumulated water between two operating points can capture rapid dry-out phenomena. Therefore, it is important to consider the operation history of cell when interpreting fuel cell data.

In conclusion, the self-heating and self-humidifying effects of passive fuel cells are balanced by the transfer of heat and water to the ambient. Optimal performance of air-breathing cells is therefore a complex function of ambient and load conditions as well as the cell design. A focus of our future efforts will be to develop an engineering model to predict performance of these cells and provide design guidelines.

References

[1] P.-W. Li, T. Zhang, Q.-M. Wang, L. Schaefer, M.K. Chyu, J. Power Sources 114 (9) (2003) 63–69.
[2] D. Chu, R. Jiang, J. Power Sources 83 (1999) 128–133.
[3] S.O. Morner, S.A. Klein, J. Sol. Energy Eng. 123 (2001) 225–231.
[4] C.K. Dyer, J. Power Sources 106 (2002) 31–34.
[5] M. Broussely, G. Archdale, J. Power Sources 136 (2) (2004) 386–394.
[6] F.P. Incropera, D.P. De Witt, Fundamentals of Heat And Mass Transfer, fourth ed., John Willey & Sons, New York, 1996, p. 487.
[7] T. Mennola, M. Noponen, M. Aronniemi, T. Hottinen, M. Nikkola, O. Himanen, P. Lund, J. Appl. Electrochem. 33 (2003) 979–987.
[8] T. Mennola, M. Noponen, T. Kallio, M. Nikkola, T. Hottinen, J. Appl. Electrochem. 34 (2004) 31–36.
[9] M. Noponen, T, Mennola, M. Mikkola, T. Hottinen, P. Lund, J. Power Sources 106 (2002) 304–312.
[10] T. Hottinen, M. Mikkola, P. Lund, J. Power Sources 129 (2004) 68–72.
[11] C. Ziegler, A. Schmitz, M. Tranitz, E. Fontes, J.O. Schumacher, J. Electrochem. Soc. 151 (12) (2004) A2028–A2041.
[12] T. Hottinen, M. Nopponen, T. Mennola, O. Himanen, M. Mikkola, P. Lund, J. Appl. Electrochem. 33 (2003) 265–271.
[13] R. O'Hayre, D. Braithwaite, W. Herman, S.J. Lee, T. Fabian, S. Cha, Y. Saito, F.B. Prinz, J. Power Sources 124 (2003) 459–472.
[14] A. Schmitz, M. Tranitz, S. Wagner, R. Hahn, C. Hebling, J. Power sources 118 (2003) 162–171.
[15] A. Schmitz, S. Wagner, R. Hahn, H. Uzn, C. Hebling, J. Power Sources 127 (2004) 197–205.
[16] F. Weinberg, Optics of Flames, Butterworth, Washington, 1963.
[17] B. Edlén, The refractive index of air, Metrologia 2 (1966).
[18] K.P. Birch, M.J. Downs, Metrologia 30 (1993).
[19] G. Bönsch, E. Potulski, Metrologia 35 (1998).
[20] Agilent Zero Volt Electronic Load, Product Note, www.agilent.com.
[21] T.E. Springer, T.A. Zawodzinsky, M.S. Wilson, S. Gottesfeld, J. Electrochem. Soc. 143 (2) (1996).
[22] M. Ciureanu, R. Roberge, J. Phys. Chem. B 105 (2001) 3531–3539.
[23] R. O'Hayre, S.W. Cha, W. Collela, F.B. Prinz, Fuel Cell Fundamentals, Willey, 2005.
[24] Y. Song, J.M. Fenton, H.R. Kunz, L.J. Bonville, M.V. Williams, J. Electrochem. Soc. 152 (3) (2005) A539–A544.
[25] J. Yu, T. Matsuura, Y. Yoshikawa, M.N. Islam, M. Hori, Phys. Chem. Chem. Phys. 7 (2005) 373–378.
[26] R.W. Lyczkowski, D. Gidaspow, AIChE J. 17 (5) (1971).
[27] Z. Qi, A. Kaufman, US patent 6,805,983 (2004).
[28] T.G. Matthews, C.V. Thompson, D.L. Wilson, A.R. Hawthorne, D.T. Mage, Environ. Int. 15 (1989) 545–550.
[29] T.L. Tatchera, A.C.K. Laia, R. Moreno-Jacksona, R.G. Sextroa, W.W. Nazaroffa, Atmos. Environ. 36 (2002) 1811–1819.
[30] T.E. Springer, T.A. Zawodzinsky, S. Gottesfeld, J. Electrochem. Soc. 138 (8) (1991).
[31] S. Slade, S.A. Campbell, T.R. Ralph, F.C. Walsh, J. Electrochem. Soc. 149 (12) (2002) A1556–A1564.